

Uncertainty Estimation for Deep Learning Image Reconstruction using a Local Lipschitz Metric

Danyal F. Bhutto^{1,2}, Bo Zhu¹, Jeremiah Z. Liu^{3,4}, Neha Koonjoo^{1,5}, Bruce R. Rosen^{1,5}, Matthew S. Rosen^{1,5,6}

¹*Athinoula A. Martinos Center for Biomedical Imaging, Department of Radiology, Massachusetts General Hospital, Charlestown, MA, United States*, ²*Boston University, Boston, MA, United States*, ³*Department of Biostatistics, Harvard University, Cambridge, MA, United States*, ⁴*Google Research, Mountain View, CA, United States*, ⁵*Harvard Medical School, Boston, MA, United States*, ⁶*Department of Physics, Harvard University, Cambridge, MA, United States*

Abstract

The use of deep learning approaches for image reconstruction is of contemporary interest in radiology, especially for approaches that solve inverse problems associated with imaging. In deployment, these models may be exposed to input distributions that are widely shifted from training data, due in part to data biases or drifts. We propose a metric based on local Lipschitz determined from a single trained model that can be used to estimate the model uncertainty for image reconstructions. We demonstrate a monotonic relationship between the local Lipschitz value and Mean Absolute Error and show that this method can be used to provide a threshold that determines whether a given DL reconstruction approach was well suited to the task. Our uncertainty estimation method can be used to identify out-of-distribution test samples, relate information regarding epistemic uncertainties, and guide proper data augmentation. Quantifying uncertainty of learned reconstruction approaches is especially pertinent to the medical domain where reconstructed images must remain diagnostically accurate.

Introduction

Imaging technologies are at the heart of medical diagnostics. From the staging and management of cancer to the functional observation of fetal cardiac health, medical imaging allows us to see inside the intact human body using spatially-encoded data acquired by sensors. Sensor domain data varies widely across imaging modalities including element-time space data (ultrasound), Radon sinogram data (X-ray CT), and k -space data (MRI). The conversion of data from the sensor domain to the image domain is a process known as image reconstruction, and typically involves the solving of an inverse problem tailored to the modality-specific details of the tomographic forward model encoding. However, image reconstruction from sensor data can be non-trivial as the inverse problem sometimes requires regularization to become well posed. Sensor datasets usually contain millions of sample values and processing all the data accurately can be a computationally challenging ad hoc set of steps. Practical issues such as errors in the MRI spatial encoding trajectory resulting from hardware imperfections or from patient motion must be managed in the reconstruction process. In the medical imaging space, with a goal of diagnostic accuracy, the reconstruction needs to occur with high confidence. As an alternative to the hand-crafted analytic approaches to image reconstruction, several efforts to apply DL to tomographic reconstruction have been described [1, 2]. In 2018, Zhu et al demonstrated the use of neural networks to perform domain-transform manifold learning and reconstruct MRI data in a single pass by a data-driven learned mapping the sensor domain into the image domain [3]. The authors demonstrated their approach to several examples of

inverse problems used in contemporary medical imaging. Their dual-domain manifold learning formalism, known as AUTOMAP, was able to learn several different forward-encoding schemes for MRI, including as Radon projection and undersampled Fourier k -space, as well as reconstruct positron emission tomography (PET) images from sinogram data. Hand-crafted reconstruction techniques can perform poorly when reconstructing real-world data with low SNR cases due to mismatch between idealized mathematical models. The AUTOMAP formalism demonstrated that a DL image reconstruction technique trained on thousands of images without any knowledge of the explicit forward-encoding Fourier model can lead to robustness in the presence of noise and consequent SNR gain [3]. Koonjoo et al also showed that a model trained on a distribution dataset that is more representative of the domain under reconstruction can perform significantly better, even when the forward-encoding model is the same in both cases. Specifically, for a reconstruction task of plant root MRI k -space data, Koonjoo et al showed that a network trained on forward-encoded synthetic roots and synthetic vascular tree structures performs significantly better than trained on a corpus of brain images [4]. Proper dataset curation is of the utmost importance as well as the ability to estimate uncertainty when a model performs poorly on an unknown distribution.

Proper uncertainty estimation is crucial for the deployment of any trained model, given the many promising applications of DL in various fields such as medicine, astronomy, and agriculture. These trained models are being deployed across all fields with high predictive accuracy mainly for classification tasks. In medicine, a few examples include detecting the risk of lung cancer [5], diagnosing Alzheimer's [6], and the detection of diabetic retinopathy [7]. Concurrently, the field of uncertainty estimation has provided multiple methods of determining the confidence of accuracy for classification tasks. Some methods include maximum SoftMax probability [8], deep ensemble [9], and Monte-Carlo dropout [10]. Especially critical in the medical field, these uncertainty estimation methods allow the proper model to be selected for deployment. Indeed, Filos et al calculated both uncertainties – aleatoric (uncertainty in the data generation that normally is not reducible) and epistemic (uncertainty from the training dataset that often is reduced by more data) – to provide a threshold for when a Bayesian DL model was well suited for real-world diabetic retinopathy scanner data or if the model displayed a high level of uncertainty, the scan to be referred to a medical expert for diagnosis [7]. We hope to use our method to perform a similar function by determining an uncertainty threshold and observing if the DL model under test performed appropriately.

Related Work

It is critical to estimate the uncertainty of DL image reconstruction models, especially in real-world clinical settings where clinical decision making depends on the accuracy of the reconstruction and where ground truth is, in most cases, unknown. Recent work has approached uncertainty estimation for DL-based image reconstruction tasks by training neural networks to output pixel-wise errors and variations. Bifurcated networks can be trained to output both a reconstructed image and a prediction of potential errors in the reconstructed image [11, 12]. Another approach is to draw parameters from a multivariate Gaussian distribution and predicted N reconstructions to estimate and quantify the pixelwise epistemic uncertainty of a trained total deep variation regularizer [13]. The benefit of these techniques is to provide radiologists a visual assessment of predicted errors contained in the reconstructed image. Unfortunately, due to learning errors caused by the training dataset only, the network may not generalize to out-of-distribution images. In a study where training datasets were shifted by a constant bias, the difference between input and output predictions was then used to quantify epistemic uncertainty. Though the authors show this

method outperforms baseline methods, they state the method cannot mitigate biases introduced by the training dataset [14].

We propose here the use of the local Lipschitz constant to measure reconstruction uncertainty. By way of definition, a function f is L -Lipschitz continuous if for any input $x, y \in \mathbb{R}^n$, there exists a nonnegative constant $L \geq 0$.

$$\|f(x) - f(y)\| \leq L\|x - y\| \quad (1)$$

The Lipschitz constant L is the maximum ratio of variations in the output space over variations in the input space. This allows the Lipschitz constant to be a measure of the sensitivity of a Lipschitz continuous function with respect to the input perturbations. The local Lipschitz constant is calculated when $y = x + e$, where e is some input perturbation such as Gaussian noise. Through comparing the difference in output to difference in input, the local Lipschitz constant corresponds to how the network weights affect the output image reconstructed and thus a measure of uncertainty caused by the network.

The use of a Lipschitz-based metric to demonstrate robustness has been studied in several works from classification to vector-to-vector regression. Several publications estimated the Lipschitz constant to demonstrate robustness to adversarial noise and use for safety verification [15–17]. Lipschitz was also used to estimate the bound for convolutional neural networks [18–20], even generalization for graphical convolutional neural networks [21]. One study placed an upper bound on the Lipschitz constant through using the activation functions as gradients of convex potential functions [22]. A study even expanded the use of the Lipschitz constant to neural networks solving vector-to-vector regression by leveraging the Lipschitz continuity properties of Mean Absolute Error (MAE) as well as its use as a generalized upper bound in the presence of additive noise [23]. Koonjoo et al calculated the Lipschitz to demonstrate local stability of AUTOMAP to stochastic perturbations of the source data [4].

Contribution. We propose a metric based on the local Lipschitz value for estimating uncertainty of DL image reconstruction techniques and demonstrate this using a single AUTOMAP model. We demonstrate the monotonic relationship between the local Lipschitz and MAE for in-distribution (ID), near out-of-distribution (NOOD), and out-of-distribution (OOD) test sets. We demonstrate how perturbation of the input with noise, similar to the local Lipschitz calculation, can be used to identify OOD test samples and outperform the baseline methods of deep ensemble and Monte-Carlo dropout. We show how a threshold can indicate whether the trained DL model reconstructed with an acceptable accuracy. Lastly, we use our method to relate information regarding epistemic uncertainties (caused by insufficient coverage of the training data) through identification of factors leading to poorer performance on certain images and guide proper training dataset curation and augmentations for more robust models. Overall, we showed that our technique is simple to implement, scalable, and easily applicable to any architecture or learned approach.

Results

Out-of-Distribution Detection. In clinical practice, the accuracy of image reconstruction is paramount and thus a technique to detect OOD test images in a real-world setting is necessary. We tested six methods of detecting OOD images and showed the receiver operating characteristic curves (ROC) and area under the curve (AUC) values in Fig 1c. When using variance values to detect OOD, by perturbing input with noise similar to local Lipschitz calculation, a single AUTOMAP model outperformed the baseline methods with an AUC of 99.97% for detecting true positives. The AUC for deep ensemble was 95.37% and for Monte-Carlo dropout was 97.43%. When using local Lipschitz values, AUTOMAP, with AUC of 86.84%, performed

comparably to the baseline methods, with AUC of 87.25% and 86.97% for deep ensemble and Monte-Carlo dropout respectively. It is important to note the baseline methods required significantly larger amount of memory and time, either to store and to inference the four models for deep ensemble, or to inference 50 times for each input and store 50 images for the Monte-Carlo dropout method. In clinical settings, computational resources are limited and when the task is to reconstruct 3D images, the baseline methods are not a favorable option. Thus, our method of perturbing the input and calculating variance is simple to perform, not computationally heavy, and outperforms the baseline methods.

Empirical Correlation. As addressed above in related work, there is theoretical evidence relating Lipschitz to MAE. Fig 2 empirically shows the monotonic relationship between our L_Φ calculations and MAE for our ID dataset for noise to signal levels $\frac{\|e\|_2}{\|x\|_2} = .05$ to 1.0. In Fig 2a, the L_Φ for each image is plotted against its MAE at each noise level, respectively. We calculated the Spearman's rank correlation coefficient for each noise level as stated in Fig 2b. There is a strong correlation between the L_Φ of each image and its MAE. At each noise level, as MAE increases, so does L_Φ . In Fig 2c, we show a histogram of L_Φ (top) and a histogram of the MAE (bottom) of the images for each noise level. With increasing noise levels, we observed that the L_Φ values increased with increasing MAE. In Extended Data Fig 1 and 2, we showed this relationship between L_Φ values and MAE and its correlation also holds for the NOOD and OOD datasets. We also observed for all datasets, as the noise level increases, the correlation increases. Thus, our method is incredibly valuable for quantifying the uncertainty of imaging modalities that suffer from high noise, such as low-field MRI.

Reconstruction benchmark. In clinical applications of DL models, the ground truth is unknown, and it becomes critical to relate uncertainty to accuracy. In Fig 3a, we hence provided and tested a pipeline that showed how our technique can be integrated in a real-world reconstruction setting and compared to a predetermined uncertainty threshold Υ . If $L_\Phi < \Upsilon$, the DL image reconstruction model performed with sufficient accuracy. If $L_\Phi \geq \Upsilon$, the data should be processed using an alternative technique. In Fig 3b and c, we performed selective prediction and demonstrated how Υ can be determined. For each noise level, we ordered the L_Φ value of each image in descending order. At each iteration, we removed the image with the highest L_Φ and referred it to be reconstructed with an alternative technique. Then, we calculated the mean L_Φ of the remaining set of images. As shown in Fig 3b, as more images are referred, the mean L_Φ of the remaining dataset decreases. In Fig 3c, we calculated the mean MAE of the corresponding remaining dataset of images, as those with the highest L_Φ were being referred at each iteration. We demonstrate the relationship that as the mean L_Φ of a dataset decreases, the mean MAE also decreases. This relationship allows us to determine a benchmark for accuracy. Radiologists can decide what accuracy is sufficient for reconstruction and the corresponding L_Φ value can be set as Υ . In Extended Data Fig 3, we demonstrate that this relationship is present for NOOD and OOD datasets as well. In practice, our local Lipschitz method can first determine OOD test images to refer to an alternative technique, as shown in Fig 1c, and then be used to benchmark if the DL model performed with sufficient accuracy on the ID or NOOD test images.

Determination of False Positives (FP) to decrease epistemic uncertainty and improve reliability. In Fig 4, we demonstrate a method to identify and train against FP. For the benchmark test to be reliable, we wanted to assess what samples lead to low L_Φ and high MAE. Fig 4a displays the L_Φ vs MAE of the OOD dataset at $\frac{\|e\|_2}{\|x\|_2} = .05$ noise to signal ratio. The red boxes in Fig 4a, b, c indicate the FP with low L_Φ ($L_\Phi < .5$) and high MAE ($MAE > .023$). In Fig 4b, we arranged the dataset with descending L_Φ and displayed

the mean L_Φ of each image. In Fig 4c, we showed the respective MAE of the corresponding images from Fig 4b. Using the L_Φ and MAE information of when FP occurred, in Fig 4d from the top row to the bottom row, we displayed the FP images, random images from the OOD dataset, and random images from the ID dataset that represents the training dataset respectively. The FP are images of high intensity and generally fill the entire space with a different FOV than the random OOD or random ID images. This additional information can lead to better training data design, decrease epistemic uncertainty caused by the incomplete training dataset, and can improve the reliability of identifying true positives using our local Lipschitz method.

Discussion

Due to its ability to increase SNR and image quality, DL is outperforming traditional techniques in reconstructing images and attracting interest from medical imaging companies and startups. Now more than ever, it becomes necessary to study the uncertainty and reliability of these techniques. Previous work relied on the training dataset and the error of their outputs and baseline methods required large amounts of computational power and memory. In this study, we developed a simple and scalable method that calculates the difference in output to the difference in input ratio to estimate the uncertainty of DL-based tomographic image reconstruction techniques. We even demonstrate how our input perturbation method, similar to local Lipschitz, can be used to identify OOD images. The local Lipschitz can benchmark whether the DL method is accurately reconstructing, or an alternative technique be used, and it can be used to identify FP to decrease epistemic uncertainty and improve reliability through guiding training data design. Though our technique applies to all image reconstruction learned approaches, we focused on the medical domain due to radiologists relying heavily on the quality of the images. We hope our technique can be used to determine if each reconstruction remains diagnostically accurate and thus patient lives are never at risk.

Methods

Notation. In image reconstruction tasks, the models employ manifold learning operating on sensor-domain data x . The task is to reconstruct $f(x)$ by learning a reconstruction mapping $\hat{f}: \mathbb{R}^{n^2} \rightarrow \mathbb{R}^{n^2}$ that minimizes loss $L(\hat{y}, y)$ where $\hat{y} = \hat{f}(x)$ is ground truth and $y = f(x)$ is prediction. The data is denoted as $\{y_i, x_i\}_i^n$ where i th observation, x_i is an $n \times n$ set of input parameters, and y_i is an $n \times n$ real set of image output values. The accuracy can be defined between the truth vector $\hat{y}_i = \{\hat{y}_1, \dots, \hat{y}_{n^2}\}$ and predicted vector $y_i = \{y_1, \dots, y_{n^2}\}$ using the Mean Absolute Error (MAE) function, $MAE(\hat{y}, y) = \frac{1}{n^2} \sum_{i=1}^{n^2} \|\hat{y}_i - y_i\|_1$.

Local Lipschitz Calculation. To calculate the local Lipschitz, we determine the upper bound caused by average case perturbations. Let us denote Φ for AUTOMAP, L_Φ for the Lipschitz constant, x for input image, and e for error. We rewrite equation 1 as follows.

$$\|\Phi(x + e) - \Phi(x)\| \leq L_\Phi \|x + e - x\| \quad (2)$$

$$\|\Phi(x + e) - \Phi(x)\| \leq L_\Phi * \|e\| \quad (3)$$

Given the small magnitude of $\|e\|$, we reorganize equation 3 and place an upper bound by empirically calculating L_Φ , where image $x' = x + e$.

$$L_\Phi \geq \frac{\|\Phi(x') - \Phi(x)\|}{\|x' - x\|} \quad (4)$$

$$L_\Phi \geq \frac{1}{n^2} \sum_{i=1}^{n^2} \frac{\|\Phi(x') - \Phi(x)\|}{\|x' - x\|} \quad (5)$$

Equation 4 lets us estimate the L_Φ for any image after we perturb it by Gaussian noise e and compare the variations in the output space over the input space. By using the mean of the difference in output to the difference in input as shown in equation 5, the L_Φ value corresponds to the effect the network has on accuracy in recreating the output since the input difference is consistent across a particular noise level. The Gaussian noise levels applied were $\frac{\|e\|_2}{\|x\|_2} = .05$ to 1.0 noise to signal ratio computed using the l_2 -norm.

Training and Testing Datasets. The training dataset was assembled from 50,000 2D T1 weighted brain magnitude-only MRIs acquired at 3T from the MGH-USC Human Connectome Project (HCP) public dataset [24]. We applied the same data augmentations detailed in the original AUTOMAP paper [3]. The final image size was 128 x 128. The corresponding k -space input was produced by forward-encoding each image with the Fast Fourier Transform using MATLAB's native 2D FFT function. The real and imaginary values of the input were separated and concatenated to produce an input vector of size 1 x 32768 per image. The target image was vectorized to size 1 x 16384. We tested our method on a wide range of distributional shifts, i.e., ID, NOOD, and OOD. The ID dataset consisted of 5,000 brain MRIs from the same HCP dataset but was not a subset of the training set. NOOD and OOD datasets consisted of 5,000 brain and 5,000 knee MRIs, respectively, from the NYU fastMRI dataset [25]. The fastMRI brain dataset consists of fully sampled images acquired at 1.5T and 3T and includes T1 weighted, T2 weighted, and FLAIR images. The knee dataset consists of images acquired at 1.5T and 3T and includes coronal proton density-weighted images with and without fat suppression, axial proton density-weighted with fat suppression, sagittal proton density, and sagittal T2 weighted with fat suppression. All fastMRI images were preprocessed using the pyFFTW, a python wrapper around the FFTW library. Even though the training data consisted of T1 weighted images, the model was able to reconstruct data acquired from a multitude of distributions due to having learned the forward-encoding well.

Architecture of neural network. There are several neural network architectures from literature to select from, including AUTOMAP [3], dAUTOMAP [26], RIM-net [27], XPDNet [28], and DAGAN [29]. In this study, we selected AUTOMAP for multiple reasons. AUTOMAP's architecture is simple to implement, consisting of two fully connected layers, two convolutional layers, and one convolutional transpose layer. The fully connected layers employ the universal approximation theorem to learn the inverse problem [30], thus the architecture is capable of learning different functions. The authors initially demonstrated AUTOMAP to reconstruct MRI, where it learned the inverse Fast Fourier Transform, and recent works have expanded its application to different domains and functions. For example, AUTOMAP has been demonstrated to learn the Biot-Savart law for quantum sensor data [31] and infrared interferometry for image reconstruction in astronomy [32]. AUTOMAP consisting of both fully connected and convolutional layers could demonstrate the universality of our uncertainty estimation technique.

The AUTOMAP GitHub code, <https://github.com/MattRosenLab/AUTOMAP>, was used as the starting point and further modified. The first fully connected layer, FC1, had 25,000 nodes with the tanh activation function. The second fully connected layer, FC2, had 16384 nodes and no activation function. The output was reshaped to size 128 x 128 for the convolutional layers. Both convolutional layers, Conv1 and Conv2, had 128 filters of size 5 x 5, with the tanh and relu activation functions respectively. The convolutional transpose layer had 1 filter of size 7 x 7 and no activation function. A stride of 1 was used across all convolutional layers with padding to not change the output shape of each layer. Our AUTOMAP architecture is shown in Fig 1a. For the deep ensemble model, we trained four individual AUTOMAP models to output four images. For the Monte-Carlo dropout model, we inserted a dropout layer, with 25% probability of randomly selecting nodes to be dropped, after the Conv1 layer as shown in Fig 1b and received comparable accuracy to the AUTOMAP model in Fig 1a.

Training details. The k -space input was noise corrupted with one percent multiplicative noise as a strategy to force the network to learn a robust internal representation and promote manifold learning. The target image was kept as ‘noise-free’. The RMSProp algorithm was used with the following parameters: learning rate = .00002, momentum = 0.0, decay = 0.9 with minibatches of size = 50. We incorporated weight regularization to all the fully connected and convolutional layers with an l_2 -norm penalty ($\lambda = .001$) to prevent overfitting, not performed in the original paper [3]. As in the original paper, an additional l_1 -norm penalty ($\gamma = .0001$) was applied to the feature map activations of the Conv2 layer to promote sparse representations. The loss function minimized was sum squared loss difference between the network output and the target image. We trained all models for 100 epochs. Each model training duration was typically 7-8 hours using TensorFlow 2.2.0 machine learning framework [33] with 2 NVIDIA Tesla GV100 graphics processing units (GPUs) with 16 GB memory capacity each.

Comparison to Baseline. To demonstrate the usefulness of our local Lipschitz calculation in determining OOD test images, we compared our method to the baseline methods of deep ensemble and Monte-Carlo dropout. For the deep ensemble model, we trained and inference four separate AUTOMAP models and calculated the local Lipschitz of the average output as well as the variance of the four images outputted by each network for all the 5000 inputs. For the Monte-Carlo dropout method, we trained one AUTOMAP model with a dropout layer. By leaving training on in inference, the dropout layer turned different nodes on and off and allowed us to receive multiple outputs for a single input. This enabled us to predict 50 images for each of the 5000 inputs and calculate the local Lipschitz and variance. Since the baseline methods output multiple images, we could calculate the variance and use that to determine OOD. For the single AUTOMAP model, we generated four outputs by perturbing the input through adding Gaussian noises of the same distribution (noise level $\frac{\|e\|_2}{\|x\|_2} = .05$) to the input and calculated the variance. To demonstrate how we could determine ID vs OOD using the local Lipschitz and variance values of each method, we generated receiver operating characteristic curves (ROC) and area under the curve (AUC) and show these results in Fig 1c.

Figures:

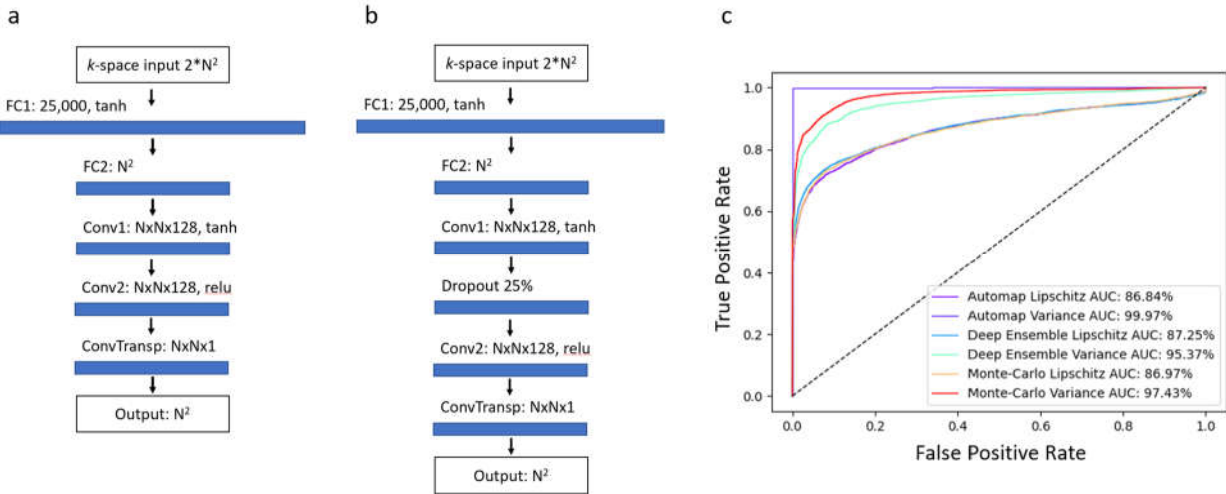


Figure 1: Out-of-Distribution Detection: a) The AUTOMAP architecture used for the single model and deep ensemble. b) AUTOMAP architecture with a dropout layer after the first convolutional layer used for the Monte-Carlo dropout method. c) Here we show the ROC and AUC values of six different methods to detect OOD images. Using the L_Φ values, a single AUTOMAP model has AUC of 86.84% in detecting OOD images, comparable to deep ensemble (AUC of 87.25%) and Monte-Carlo dropout (AUC of 86.97%). The variance of output images of each method was used for OOD detection. By adding different noises of the same distribution (noise to signal level $\frac{\|e\|_2}{\|x\|_2} = .05$), we reconstruct the same image and calculate the variance for the single AUTOMAP model. AUTOMAP with variance had AUC of 99.97% and outperformed deep ensemble (AUC of 95.37%) and Monte-Carlo dropout (AUC of 97.43%).

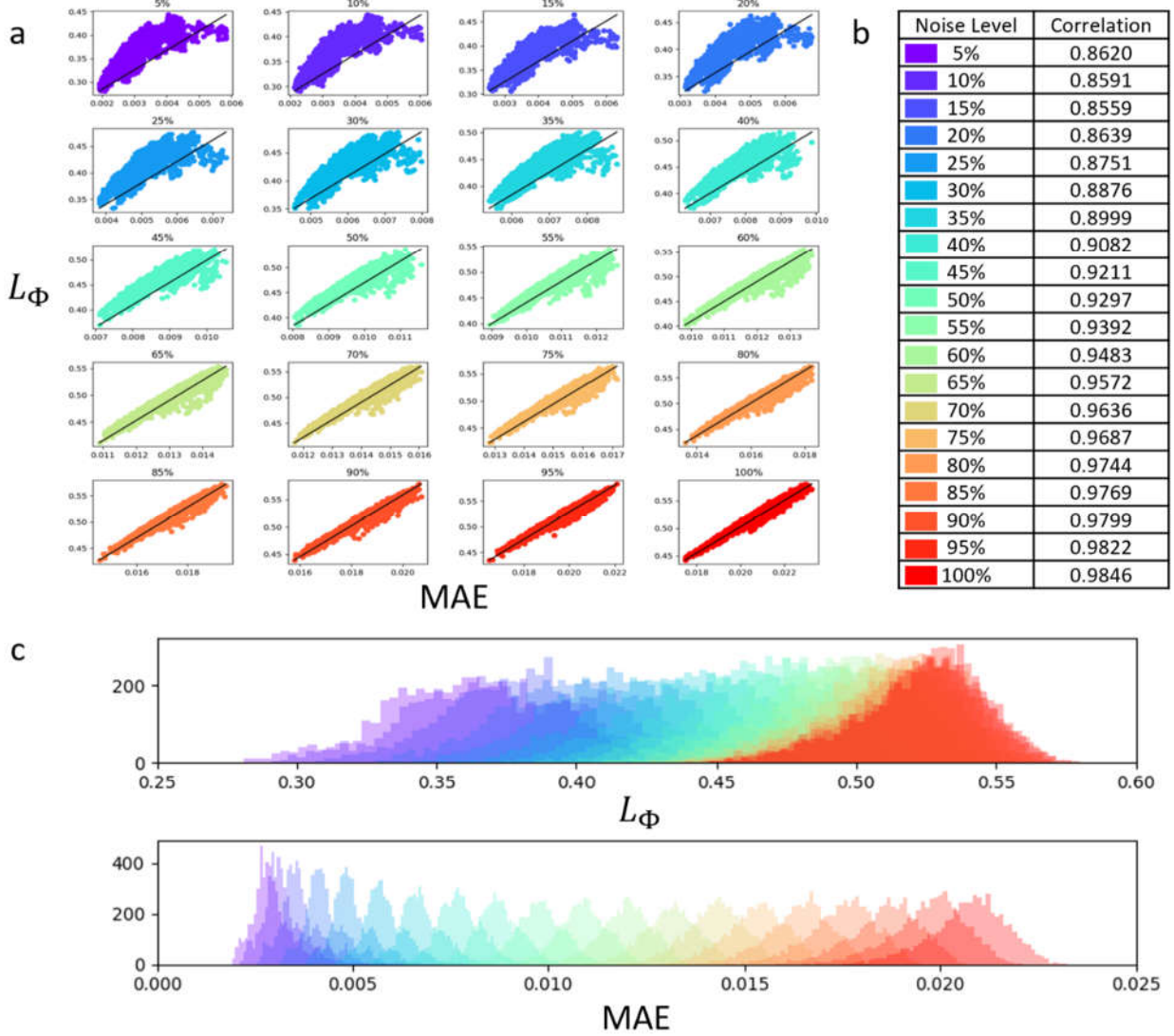


Figure 2: Empirical study of the monotonic relationship between L_Φ and MAE for ID dataset for noise levels from 5% to 100%. a) represents the 20 different plots of the L_Φ for each image against MAE value. Each plot corresponds to 5000 images in total at 20 different noise levels ranging from 5% to 100%. The noise levels indicated on the top of each graph and are color-coded from indigo (top left plot) to red (bottom right plot). The trend on each plot indicates that as MAE increases, the L_Φ increases as well. b) Table of the Spearman correlation values at each noise level. The values show a strong correlation between L_Φ for each image and its MAE value. c) L_Φ histogram (top) and the MAE histogram (bottom) of the 5000 images for each noise level are shown plotted using the same color scale. Both histograms demonstrate the relationship between L_Φ and MAE that as MAE increases due to increased noise levels, so does L_Φ , and thus holds for noisy imaging modalities as well.

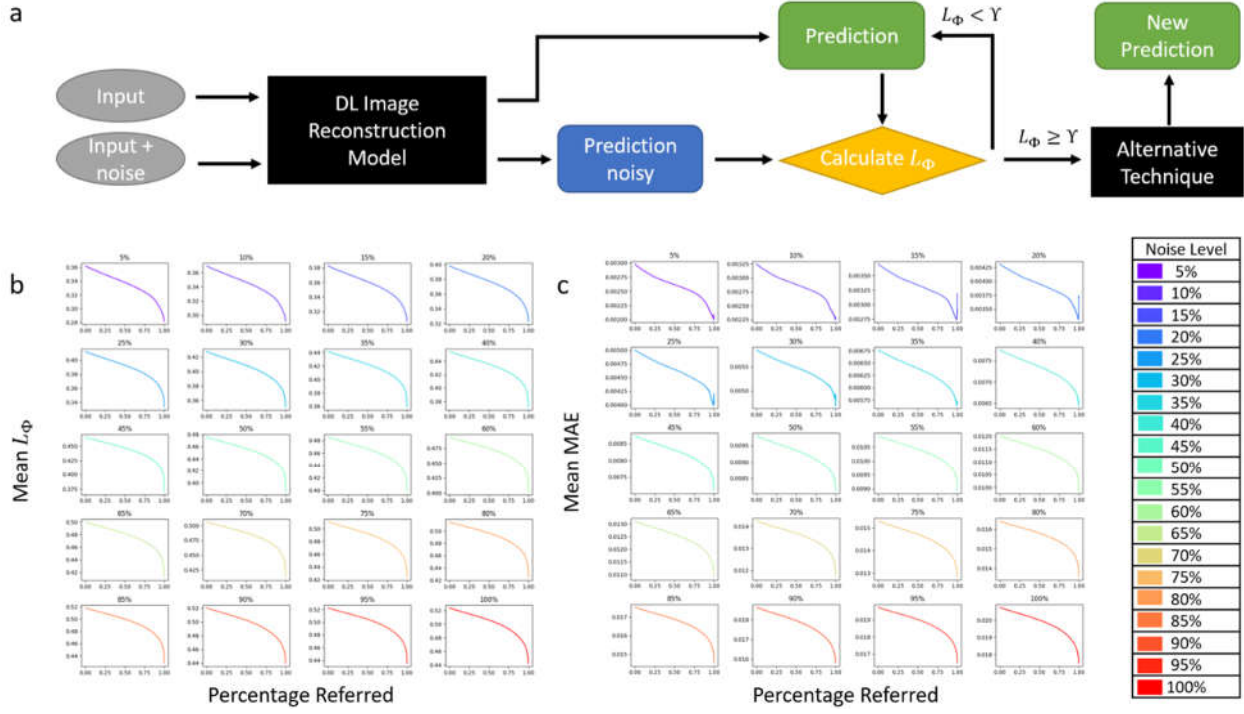


Figure 3: Reconstruction benchmark: a) Schematic of the image reconstruction pipeline used to determine the local Lipschitz value. For a given test image, the trained DL image reconstruction model predicts a clean and noisy image, and then these are used to calculate L_Φ . If L_Φ is below a predetermined threshold γ , then the DL model performed well. If L_Φ is above the threshold γ , there is greater uncertainty than desired and an alternative technique to reconstruct the image should be used. b) and c) A selective prediction was performed to determine the threshold γ at 20 different noise levels. The same color codes for the noise levels were used. L_Φ was sorted in descending order with their corresponding MAE, respectively. At all noise levels, mean MAE decreases as more images with the highest L_Φ are referred to an alternative technique. Based on an acceptable MAE determined by a radiologist, a corresponding threshold γ can be determined based on the percentage referred.

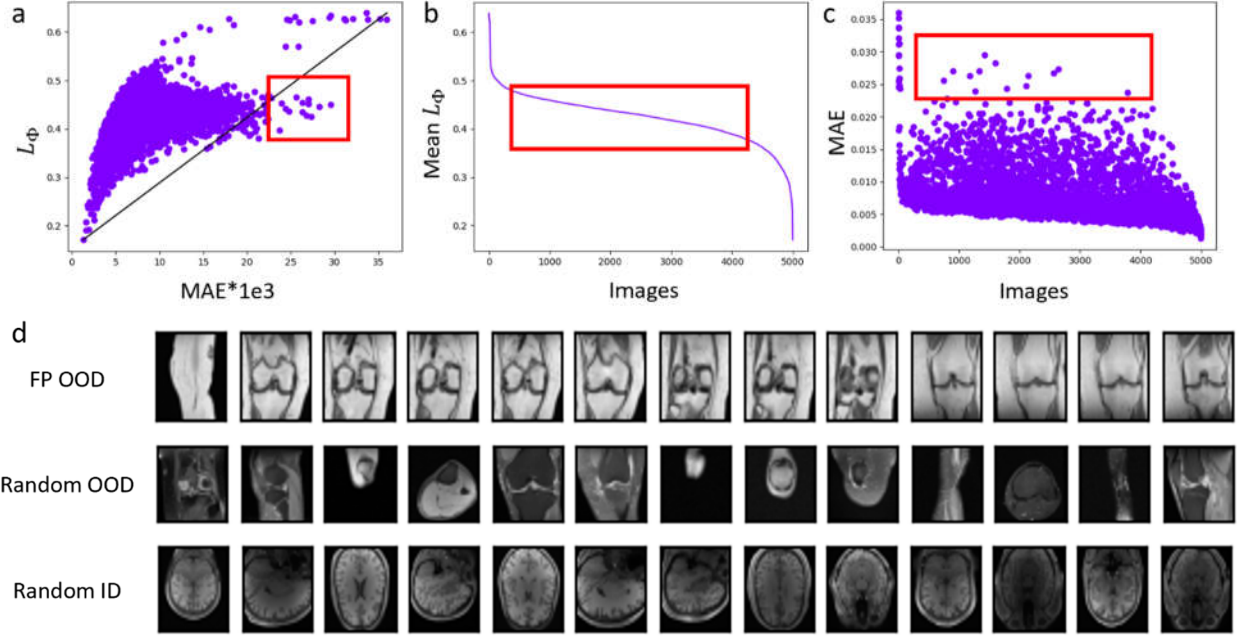
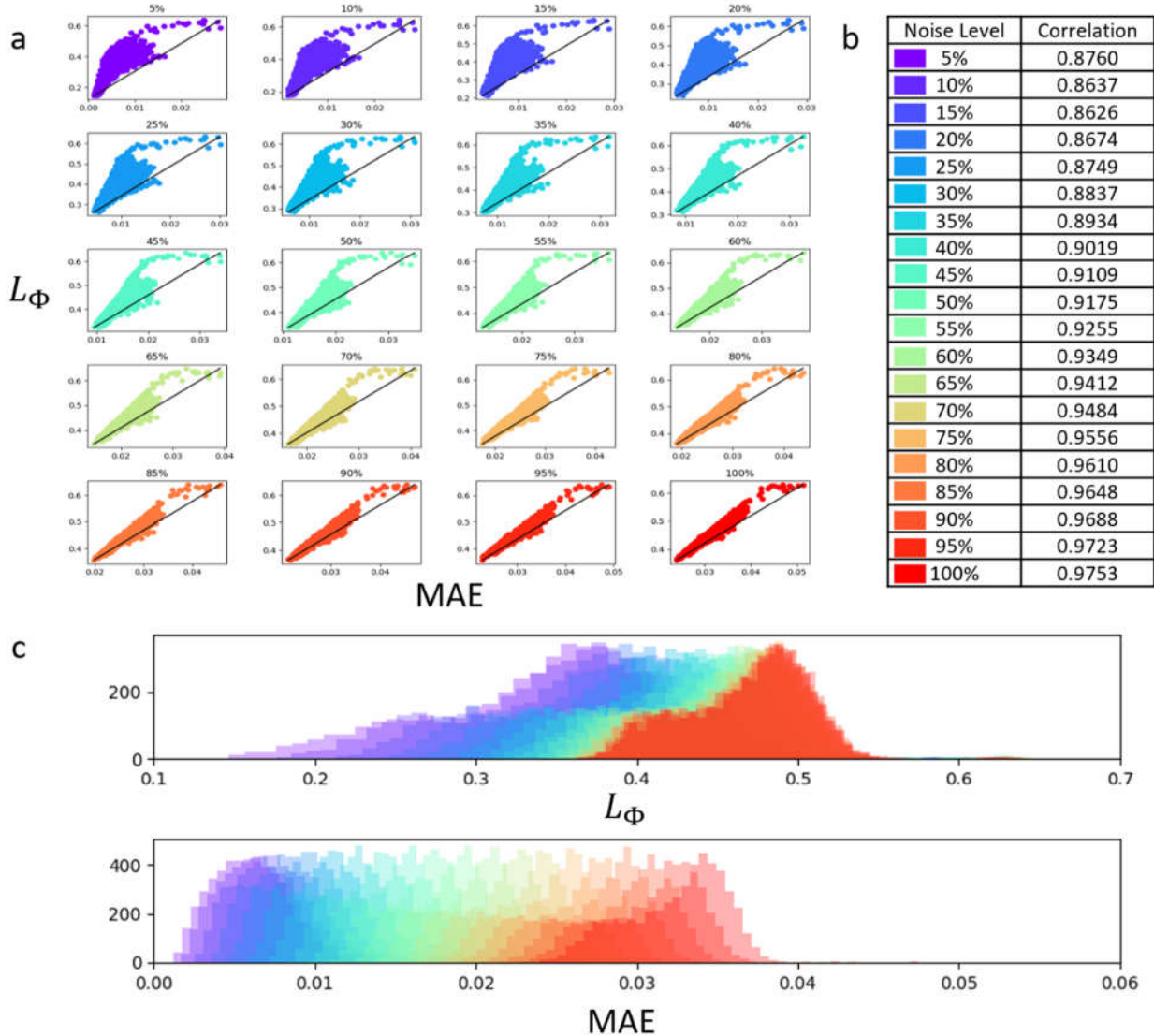
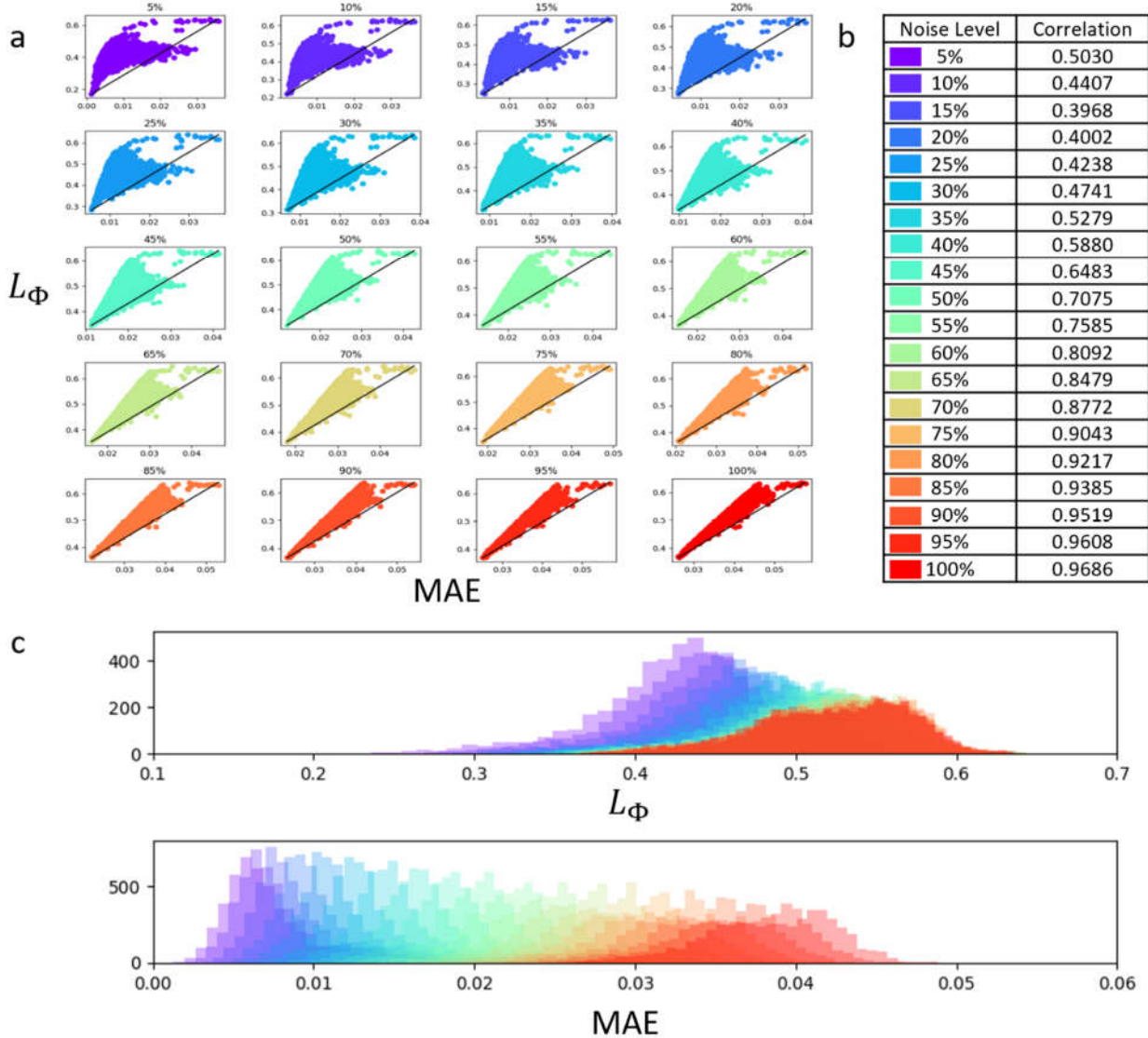


Figure 4: Determination of False Positives (FP) to decrease epistemic uncertainty and improve reliability: a) we display the L_Φ vs MAE of the OOD dataset at 5% noise. In b), the dataset was rearranged with descending L_Φ and the mean L_Φ is displayed. In c), the respective MAE value of each of the 5000 images from plot b) are plotted. The red boxes in a), b), and c) indicate the FP samples with low L_Φ ($L_\Phi < .5$) and high MAE ($MAE > .023$). d) (from the top row to the bottom row) - FP images, random images from the OOD dataset, and random images from the ID dataset that represents the training dataset are displayed. The FP are images of high intensity and fill the entire space with a different FOV than the random OOD or random ID images. This allows us to better augment the training data and decrease the epistemic uncertainty, so the model performs well, and the number of FP samples decreases.

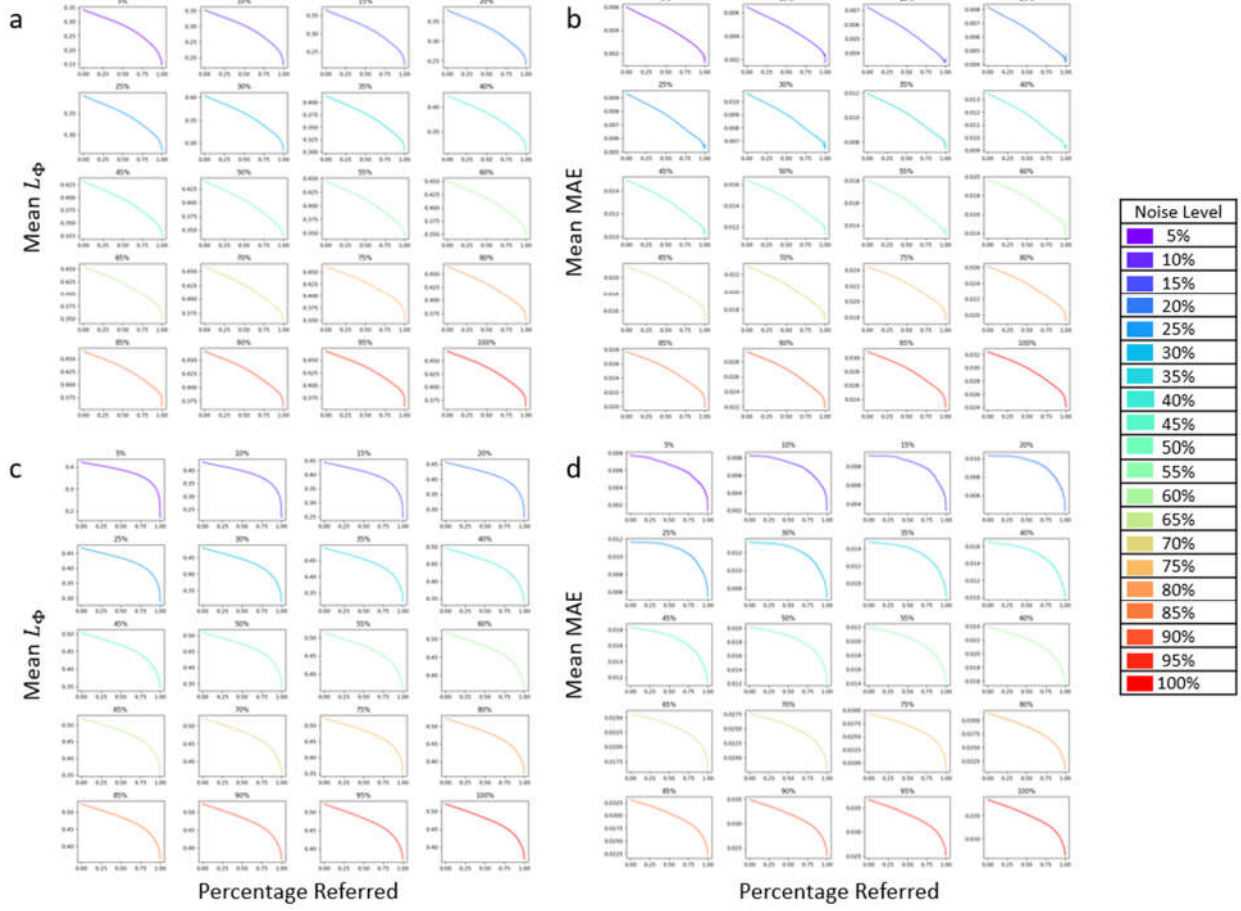
Extended Data Figures:



Extended Data Figure 1: Empirical study of the monotonic relationship between L_Φ and MAE for the NOOD dataset with brain images from the fastMRI dataset at noise levels from 5% to 100%. a) represents the 20 different plots of the L_Φ for each image against MAE value. Each plot corresponds to 5000 images in total. The noise levels indicated on the top of each graph and are color-coded from indigo (top left plot) to red (bottom right plot). The trend on each plot shows that as MAE increases, the L_Φ increases as well. b) states the Spearman correlation values at each noise level. The values show a strong correlation between L_Φ for each image and its MAE value. c) Two histograms are depicted. The L_Φ histogram (top) and the MAE histogram (bottom) of the 5000 images for each noise level, where the same color code was used. Both histograms demonstrate the relationship between L_Φ and MAE that as MAE increases due to increased noise levels, so does L_Φ .



Extended Data Figure 2: Empirical study of the monotonic relationship between L_Φ and MAE for the OOD dataset with knee images from the fastMRI dataset at noise levels from 5% to 100%. a) represents the 20 different plots of the L_Φ for each image against MAE value. Each plot corresponds to 5000 images in total. The noise levels indicated on the top of each graph and are color-coded from indigo (top left plot) to red (bottom right plot). The trend on each plot shows that as MAE increases, the L_Φ increases as well. b) states the Spearman correlation values at each noise level. The values show a moderate correlation that becomes strong, as noise levels are increased, between L_Φ for each image and its MAE value. c) Two histograms are depicted. The L_Φ histogram (top) and the MAE histogram (bottom) of the 5000 images for each noise level, where the same color code was used. Both histograms demonstrate the relationship between L_Φ and MAE that as MAE increases due to increased noise levels, so does L_Φ .



Extended Data Figure 3: Selective prediction for NOOD and OOD datasets: a) and b) demonstrate selective prediction for the NOOD dataset. As images of high L_Φ values are referred to an alternative method, the corresponding MAE of the remaining dataset also decreases. This relationship is also true for the OOD dataset as shown in c) and d). We observe this relationship for all noise levels.

References

1. Arridge S, Maass P, Öktem O, Schönlieb C-B. Solving inverse problems using data-driven models. *Acta Numer* 2019; 28: 1–174.
2. Wang G, Ye JC, Man BD. Deep learning for tomographic image reconstruction. *Nat Mach Intell* 2020; 2: 737–748.
3. Zhu B, Liu JZ, Cauley SF, Rosen BR, Rosen MS. Image reconstruction by domain-transform manifold learning. *Nature* 2018; 555: 487–492.
4. Koonjoo N, Zhu B, Bagnall GC, Bhutto D, Rosen MS. Boosting the signal-to-noise of low-field MRI with deep learning image reconstruction. *Sci Rep-uk* 2021; 11: 8248.
5. Ardila D, Kiraly AP, Bharadwaj S, Choi B, Reicher JJ, Peng L, et al. End-to-end lung cancer screening with three-dimensional deep learning on low-dose chest computed tomography. *Nat Med* 2019; 25: 954–961.
6. Qiu S, Joshi PS, Miller MI, Xue C, Zhou X, Karjadi C, et al. Development and validation of an interpretable deep learning framework for Alzheimer’s disease classification. *Brain* 2020; 143: 1920–1933.
7. Filos A, Farquhar S, Gomez AN, Rudner TGJ, Kenton Z, Smith L, et al. A Systematic Comparison of Bayesian Deep Learning Robustness in Diabetic Retinopathy Tasks. *Arxiv* 2019.
8. Hendrycks D, Gimpel K. A Baseline for Detecting Misclassified and Out-of-Distribution Examples in Neural Networks. *Arxiv* 2016.
9. Lakshminarayanan B, Pritzel A, Blundell C. Simple and Scalable Predictive Uncertainty Estimation using Deep Ensembles. *Arxiv* 2016.
10. Gal Y, Ghahramani Z. Dropout as a Bayesian Approximation: Representing Model Uncertainty in Deep Learning. *Arxiv* 2015.
11. Barbano R, Kereta Ž, Zhang C, Hauptmann A, Arridge S, Jin B. Quantifying Sources of Uncertainty in Deep Learning-Based Image Reconstruction. *Arxiv* 2020.
12. Shaw R, Sudre CH, Ourselin S, Cardoso MJ. Estimating MRI Image Quality via Image Reconstruction Uncertainty. *Arxiv* 2021.
13. Narnhofer D, Effland A, Kobler E, Hammernik K, Knoll F, Pock T. Bayesian Uncertainty Estimation of Learned Variational MRI Reconstruction. *Arxiv* 2021.
14. Thiagarajan JJ, Anirudh R, Narayanaswamy V, Bremer P-T. Single Model Uncertainty Estimation via Stochastic Data Centering. *Arxiv* 2022.

15. Weng T-W, Zhang H, Chen P-Y, Yi J, Su D, Gao Y, et al. Evaluating the Robustness of Neural Networks: An Extreme Value Theory Approach. *Arxiv* 2018.
16. Weng T-W, Zhang H, Chen H, Song Z, Hsieh C-J, Boning D, et al. Towards Fast Computation of Certified Robustness for ReLU Networks. *Arxiv* 2018.
17. Ruan W, Huang X, Kwiatkowska M. Reachability Analysis of Deep Neural Networks with Provable Guarantees. *Arxiv* 2018.
18. Balan R, Singh M, Zou D. Lipschitz Properties for Deep Convolutional Networks. *Arxiv* 2017.
19. Zou D, Balan R, Singh M. On Lipschitz Bounds of General Convolutional Neural Networks. *Arxiv* 2018.
20. Bartlett P, Foster DJ, Telgarsky M. Spectrally-normalized margin bounds for neural networks. *Arxiv* 2017.
21. Verma S, Zhang Z-L. Stability and Generalization of Graph Convolutional Neural Networks. *Arxiv* 2019.
22. Fazlyab M, Robey A, Hassani H, Morari M, Pappas GJ. Efficient and Accurate Estimation of Lipschitz Constants for Deep Neural Networks. *Arxiv* 2019.
23. Qi J, Du J, Siniscalchi SM, Ma X, Lee C-H. On Mean Absolute Error for Deep Neural Network Based Vector-to-Vector Regression. *Ieee Signal Proc Let* 2020; 27: 1485–1489.
24. Fan Q, Witzel T, Nummenmaa A, Dijk KRAV, Horn JDV, Drews MK, et al. MGH–USC Human Connectome Project datasets with ultra-high b-value diffusion MRI. *Neuroimage* 2016; 124: 1108–1114.
25. Zbontar J, Knoll F, Sriram A, Murrell T, Huang Z, Muckley MJ, et al. fastMRI: An Open Dataset and Benchmarks for Accelerated MRI. *Arxiv* 2018.
26. Schlemper J, Oksuz I, Clough JR, Duan J, King AP, Schnabel JA, et al. dAUTOMAP: decomposing AUTOMAP to achieve scalability and enhance performance. *Arxiv* 2019.
27. Lønning K, Putzky P, Sonke J-J, Reneman L, Caan MWA, Welling M. Recurrent inference machines for reconstructing heterogeneous MRI data. *Med Image Anal* 2019; 53: 64–78.
28. Ramzi Z, Ciuciu P, Starck J-L. XPDNet for MRI Reconstruction: an application to the 2020 fastMRI challenge. *Arxiv* 2020.
29. Yang G, Yu S, Dong H, Slabaugh G, Dragotti PL, Ye X, et al. DAGAN: Deep De-Aliasing Generative Adversarial Networks for Fast Compressed Sensing MRI Reconstruction. *Ieee T Med Imaging* 2017; 37: 1310–1321.
30. Hornik K, Stinchcombe M, White H. Multilayer feedforward networks are universal approximators. *Neural Networks* 1989; 2: 359–366.

31. Ku M, Turner M, Bhutto D, Zhu B, Rosen M, Walsworth R. Machine learning the Biot-Savart law from quantum sensor data. *APS March Meeting*. 2021. pp S61-004.
32. Sanchez-Bermudez J, Alberdi A, Schödel R, Sivaramakrishnan A. CASSINI-AUTOMAP: a novel image reconstruction algorithm for infrared interferometry. *Opt Infrared Interf Imaging Viii* 2022; 12183: 121831K-121831K-14.
33. Abadi M, Agarwal A, Barham P, Brevdo E, Chen Z, Citro C, et al. TensorFlow: Large-Scale Machine Learning on Heterogeneous Distributed Systems. *Arxiv* 2016.